Supplementary Information
Observation of Electronic Viscous Dissipation in Graphene Magneto-thermal Transport

Artem Talanov*,[1,2] Jonah Waissman*,[1,3] Aaron Hui,[4] Brian Skinner,[4] Kenji Watanabe,[5] Takashi Taniguchi,[5] and Philip Kim[1,2]

[1] *Department of Physics, Harvard University, Cambridge, Massachusetts 02138, USA*
[2] *John A. Paulson School of Engineering and Applied Sciences, Harvard University, Cambridge, MA 02138, USA*
[3] *Institute of Applied Physics, The Hebrew University of Jerusalem, Jerusalem 9190401, Israel*
[4] *Department of Physics, Ohio State University, Columbus, Ohio 43202, USA*
[5] *National Institute for Material Science, 1-1 Namiki, Tsukuba 305-0044, Japan*

CONTENTS

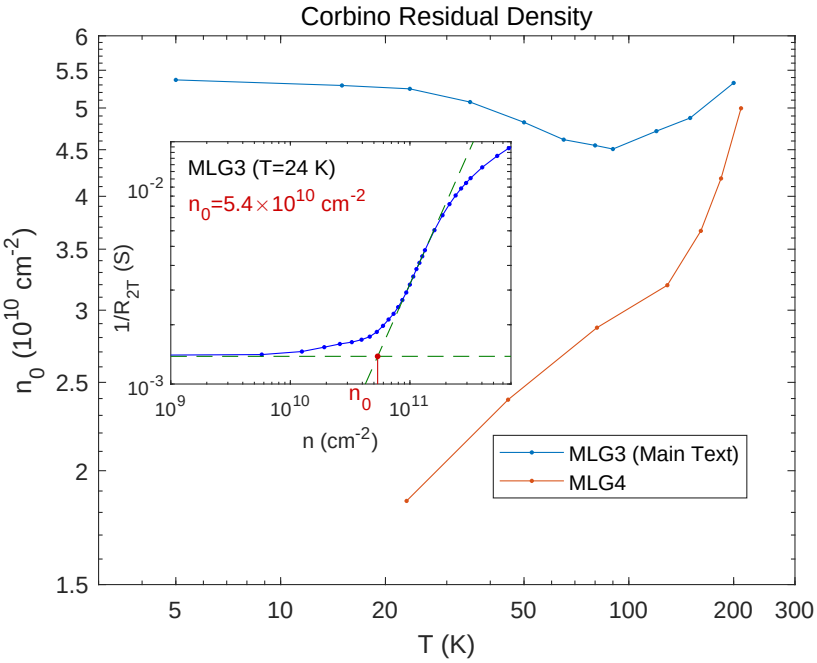

FIG. S1. Main panel: Residual density of both devices in this work. Inset: log-log plot of electrical conductance vs n (blue). Extrapolations to the linear and flat parts are indicated by the green dashed lines. Red indicates the intersection of these, which is the residual density n_0.

I. DEVICE DISORDER AND RESIDUAL DENSITY

Here, we present measurement of the device disorder level. Figure S1 shows the residual density versus temperature for both devices exhibited in this work.

II. RESULTS FOR AN ADDITIONAL DEVICE

In this section, we present data from a second monolayer graphene Corbino device. For this device, the measured transport ratio does not show an absolute suppression $G_{th,gen}/12G_{el}\mathcal{L}_0T_{bath} < 1$, only a relative suppression. Nonetheless, this relative suppression is observed in the degenerate $T < T_F$ and quasi-elastic $T > T_{BG}$ region of the parameter space, similar to the device of the main text. This device has a shorter channel length of ~ 1.64 μm. The shorter channel length and smaller radii compared to the device shown in the main text result in a larger region of expected viscous behavior, since the device dimensions are even smaller than the Gurzhi length l_G compared to the first device. Figure S2 shows the two devices, and compares their electrical resistance and Lorenz ratio versus density for varying temperature. We observe similar Dirac peak behavior, and comparable transport ratio behavior with the zero density peak, relative suppression for moderate densities, and enhancement at large densities (see main text and below). Figure S4 shows the electrical and thermal magnetoresistance (EMR and TMR) parabolic prefactors A_{el} and A_{th}, respectively, versus density for selected temperatures, compared to the zero-field transport ratio. Here, we observe a similar emergence of negative TMR corresponding with the relative suppression of the zero-field transport ratio in density and temperature. Figure S5 shows zero-field transport ratios and the parabolic prefactor ratio A_{th}/A_{el} versus density and temperature, showing the emergence of the relative suppression and negative TMR regions in the degenerate and quasi-elastic regime, as seen in the device discussed in the main text.

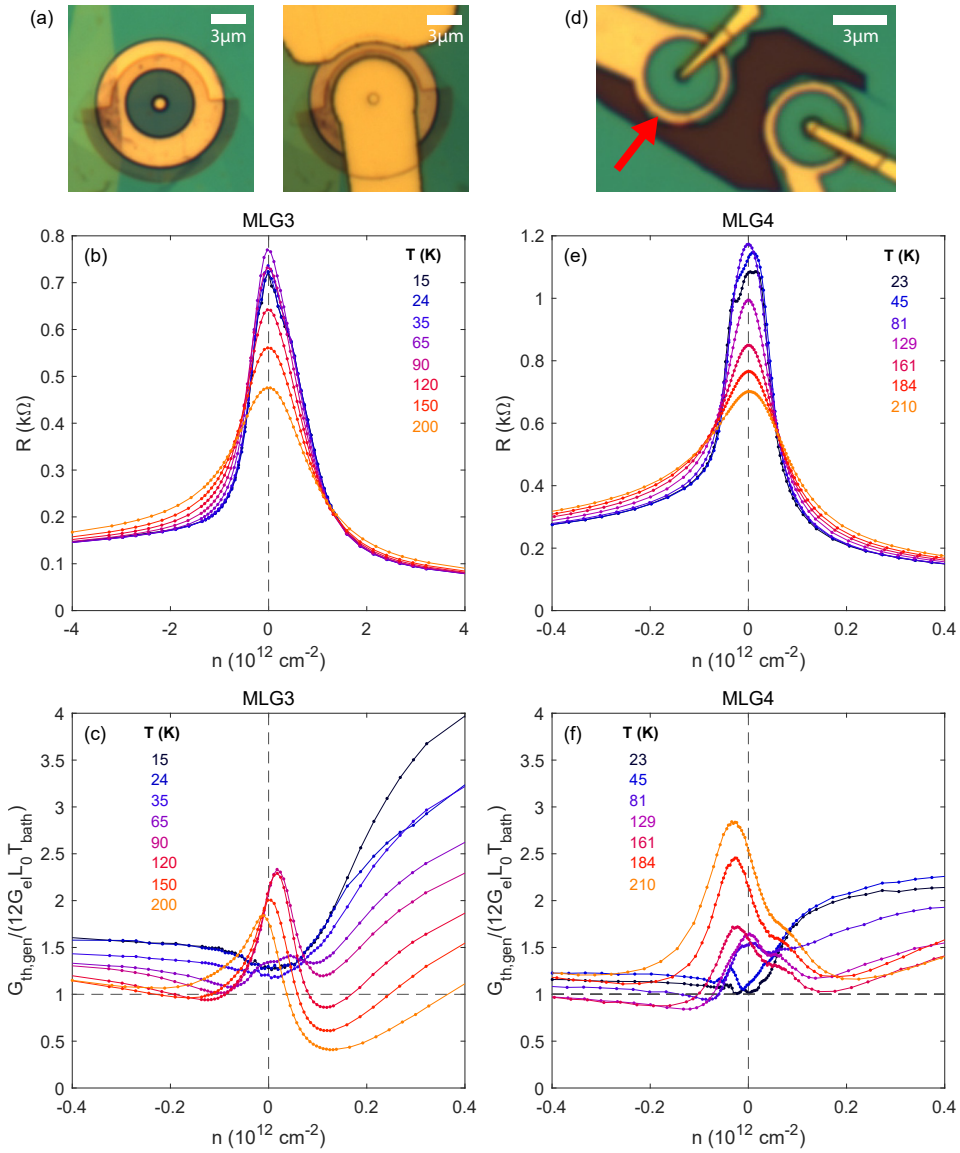

FIG. S2. a) Optical micrograph of the device shown in the main text (MLG3), before (left) and after (right) deposition of the central contact lead. b) Electrical resistance R of MLG3 versus density n for varying bath temperatures T. c) Transport ratio $G_{th,gen}/12G_{el}\mathcal{L}_0 T_{bath}$ versus n for varying T. d) Optical micrograph of a second Corbino device (MLG4) (left device, red arrow). e) R versus n for varying T for MLG4. f) Transport ratio $G_{th,gen}/12G_{el}\mathcal{L}_0 T_{bath}$ versus n for varying T for MLG4.

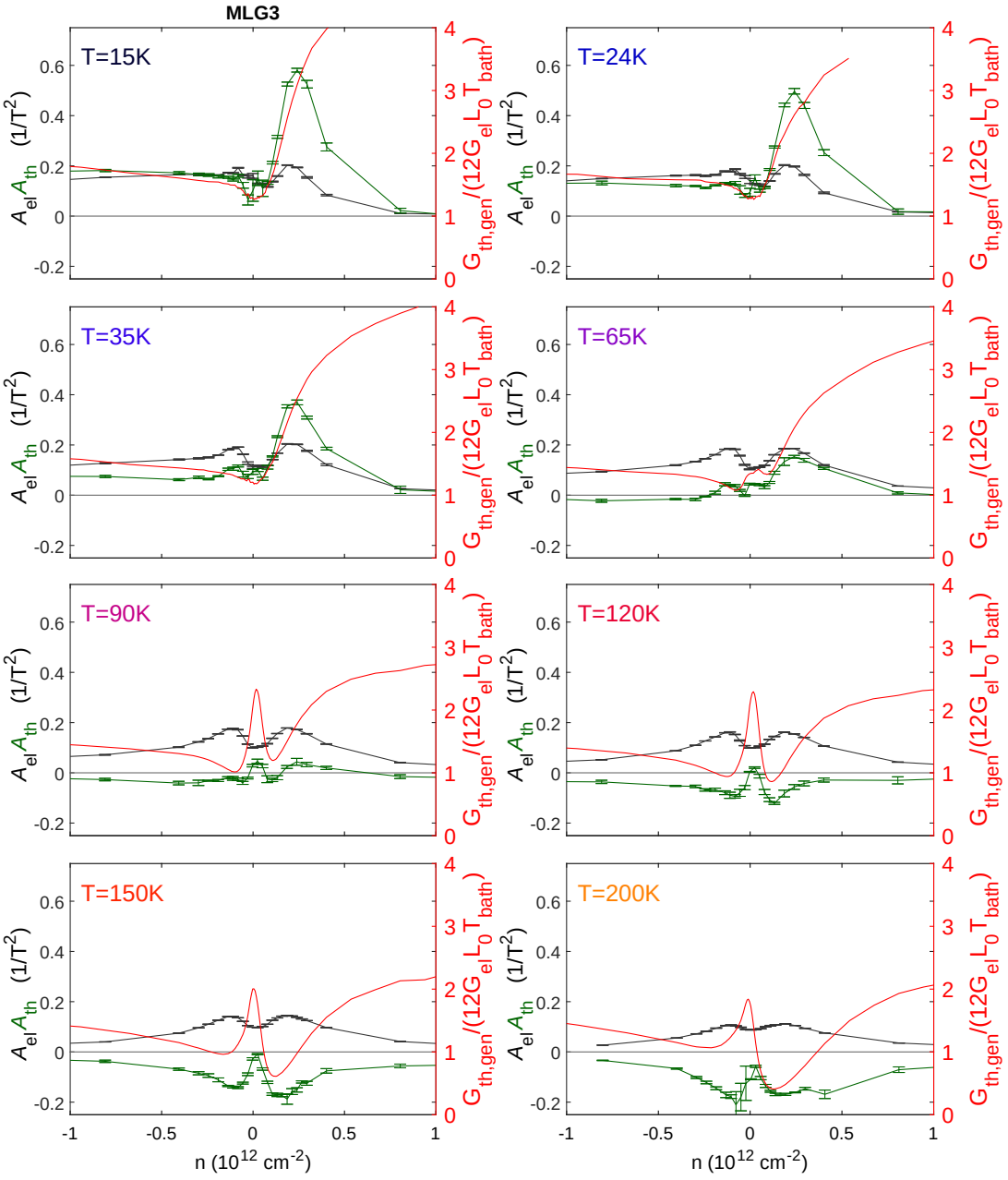

FIG. S3. Left axes: Line cuts of A_{el} (dark green) and A_{th} (light green) versus n for varying T from main text device MLG3. Right axis: Line cuts of $G_{th,gen}/12G_{el}\mathcal{L}_0T_{bath}$ versus n. See main text.

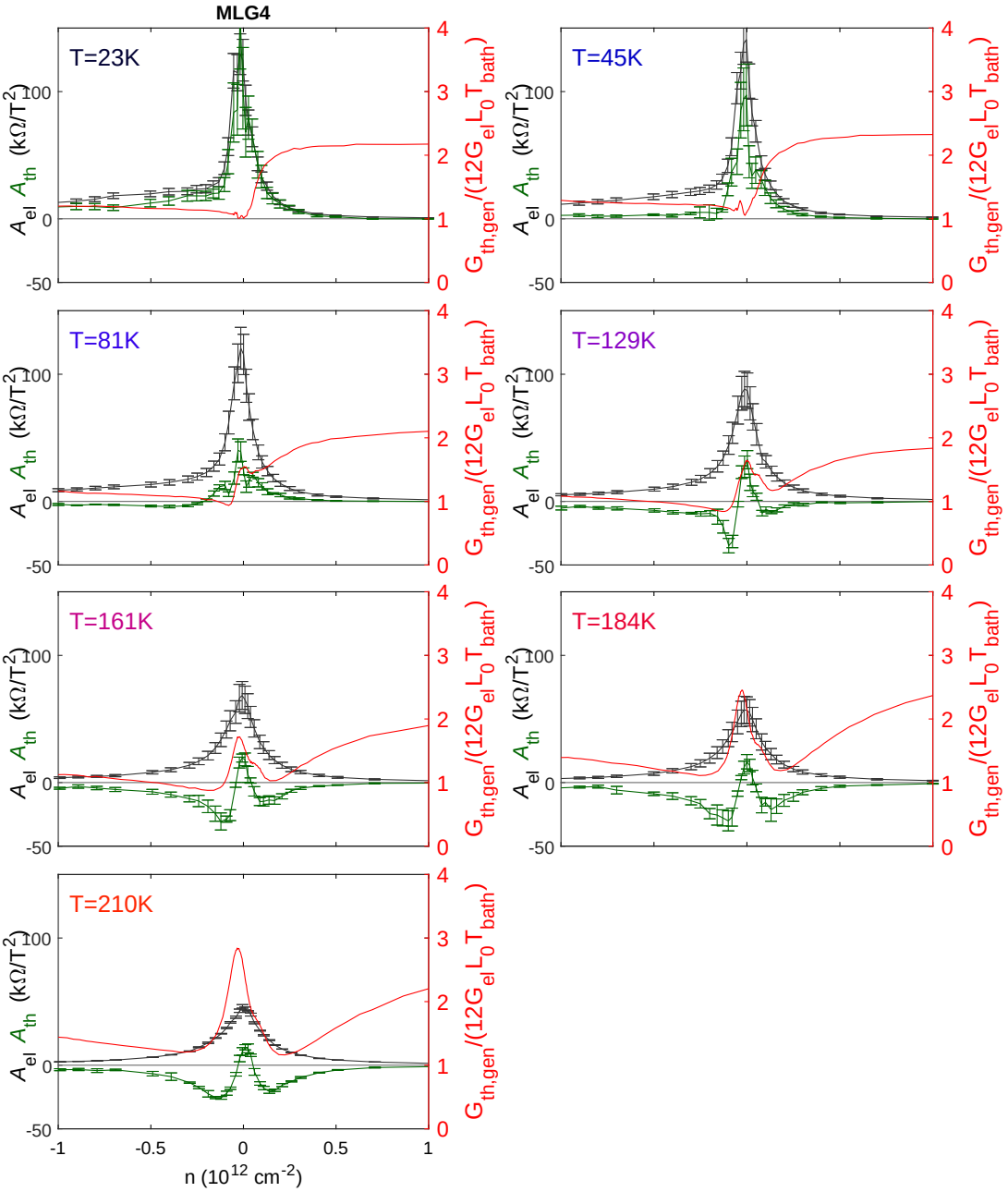

FIG. S4. Left axes: Line cuts of A_{el} (dark green) and A_{th} (light green) versus n for varying T from additional device MLG4. Right axis: Line cuts of $G_{th,gen}/12G_{el}\mathcal{L}_0T_{bath}$ versus n. See main text.

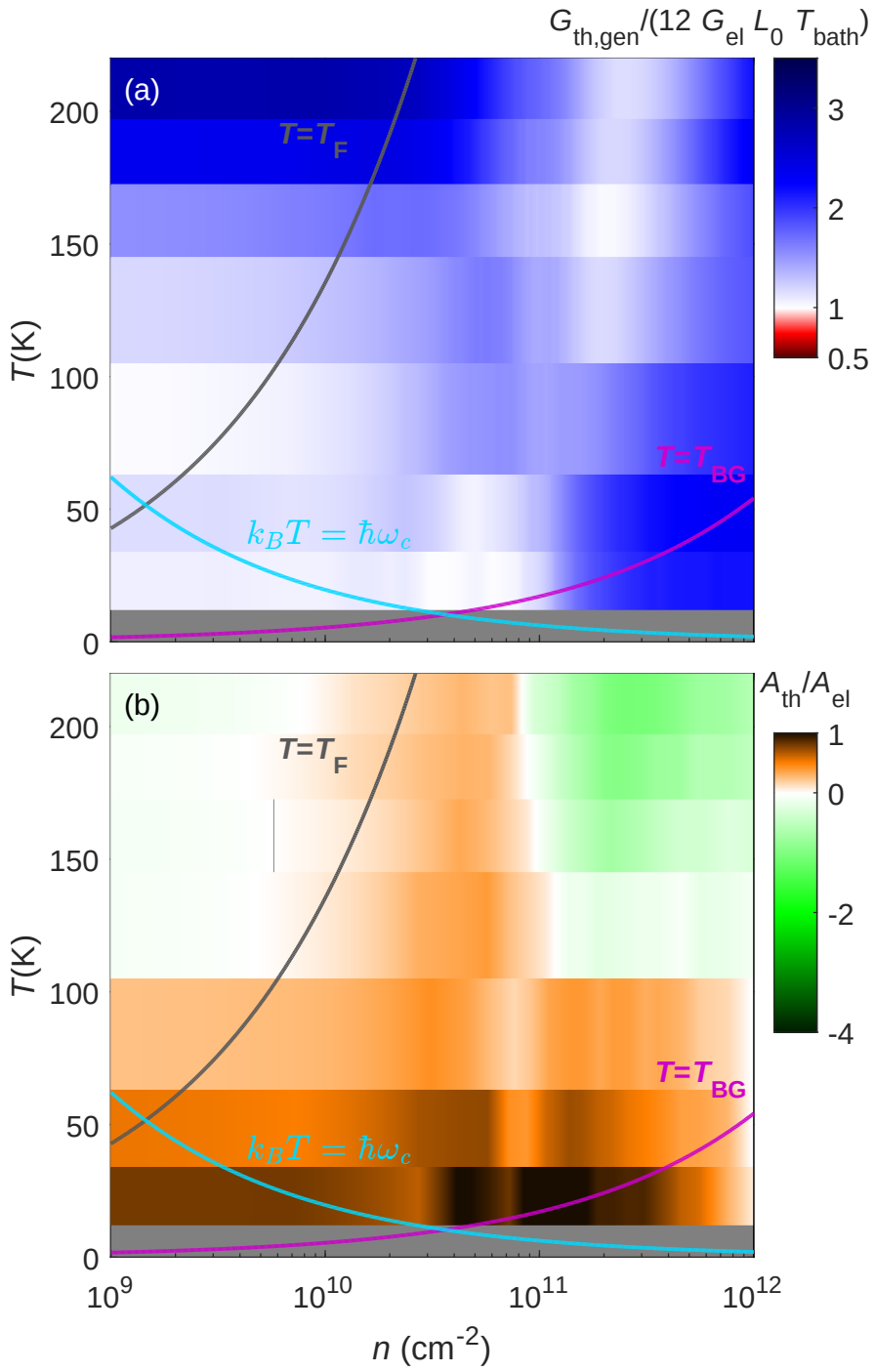

FIG. S5. a) Transport ratio $G_{th,gen}/12G_{el}\mathcal{L}_0T_{bath}$ versus density n and temperature T for additional device MLG4 at $B = 0$. Grey line: $T = T_F$ the Fermi temperature. Magenta line: T_TBG, the Bloch-Gruneisen temperature. Cyan line: cyclotron energy in temperature units. See main text. b) Ratio of thermal magnetoresistance curvature A_{th} to electrical magnetoresistance curvature A_{el} versus n and T.

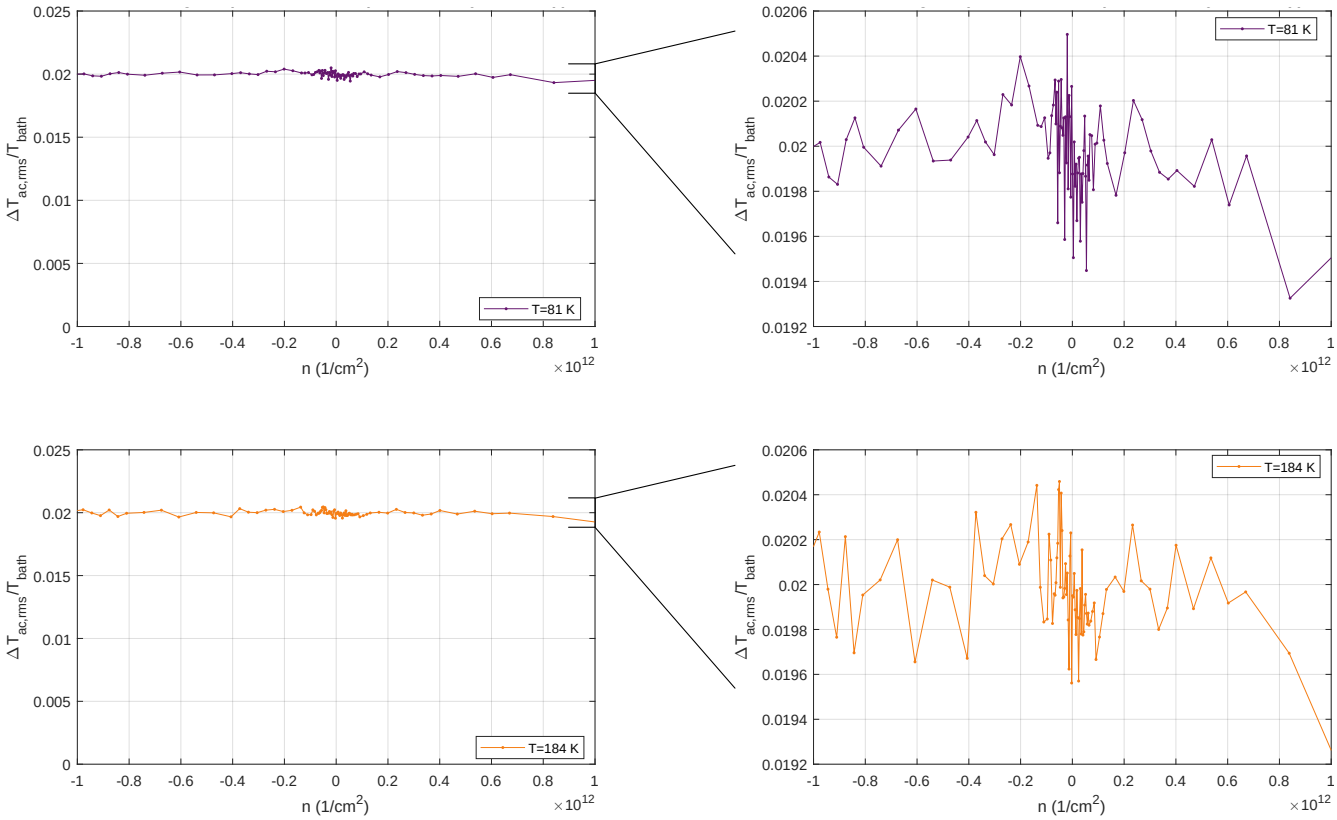

FIG. S6. Normalized temperature modulation $\Delta T_{ac,rms}/T_{bath}$ versus n for two representative T_{bath}.

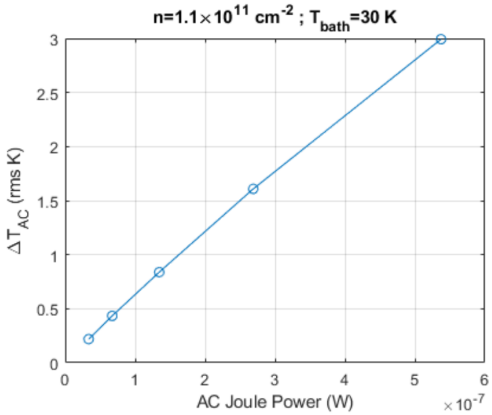

FIG. S7. Normalized temperature modulation $\Delta T_{ac,rms}/T_{bath}$ versus applied Joule power for $T_{bath} = 30K$ and $n = 1.1 \times 10^{11}\ cm^{-2}$.

III. RAW TEMPERATURE DATA

Our measurements operate under an open-loop feedback mechanism that holds $\Delta T/T$ fixed to between $2-5\%$ in these measurements, where ΔT is the measured electronic temperature rise and T is the bath temperature. These temperature changes are chosen to be in the linear response regime according to sweeps of ΔT vs P_J sweeps, where

P_J is the injected Joule power. The typical bias current has a range of $\sim 70-280\ \mu A$ at $200K$ and $\sim 1.5-110\ \mu A$ at $15K$, varying as needed for the power to maintain a few percent temperature increase. At higher bath temperatures more current is needed to achieve a given $\Delta T/T$ for higher electron densities than the system was able to provide, with the maximum available being $\sim 280\ \mu A$; this is why the range is much larger for $200K$ than $15K$. Figure S6 shows the measured temperature rise normalized by the bath temperature $\Delta T/T$, for two representative temperatures at $B = 0$, for device MLG4. For this sweep, $\Delta T/T$ 2% .

In Fig.S7, we show $\Delta T/T$ versus the applied Joule power, for $T_{bath} = 30K$ and $n = 1.1 \times 10^{11}\ cm^{-2}$. At the chosen operating point of $\Delta T/T$ 2%, we are deep in the linear response regime.

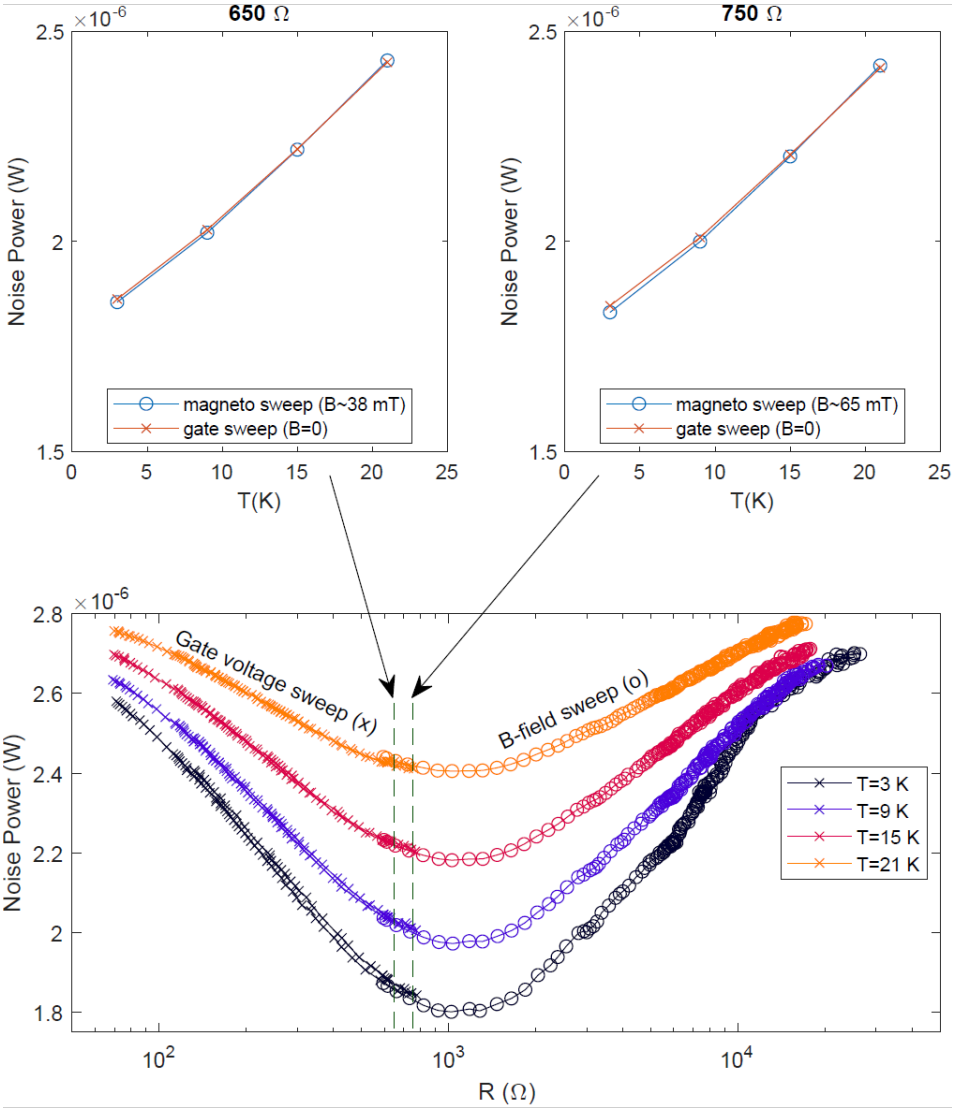

FIG. S8. Upper left: noise power vs. bath temperature at a sample resistance of 650Ω at $B = 0$ (x symbols) and $B = 38mT$ (o symbols). Upper right: noise power vs. bath temperature at a sample resistance of 750Ω at $B = 0$ (x symbols) and $B = 65mT$ (o symbols). Lower panel: noise power versus sample resistance, for varying bath temperature. The functional form of the fit is given in [1]. The sample resistance is swept by gate voltage at low resistances, and by magnetic field at high resistance. In the overlap region, the two data sets coincide, demonstrating that the measurement circuit is not influenced by the magnetic field (see discussion).

IV. VERIFYING MAGNETIC FIELD-INDEPENDENCE OF THE MEASUREMENT CIRCUIT

We have carefully designed our measurement circuits to avoid influence by the external magnetic field [1]. The impedance matching circuit is created with air-core inductors and ceramic or silicon chip capacitors that do not have magnetic field or temperature dependence. Our amplifiers are situated far outside the field range, outside the cryostat, with separate cryogenic cooling. In this work, the maximum field attained is 130 mT. To experimentally verify that there is no impact of the magnetic field on the Johnson noise circuit, we present data from our noise calibration in

Fig. S8. In the data shown, we measure the raw output noise power versus the bath temperature. We take many such curves for different values of the gate voltage and magnetic field, while measuring the sample electrical resistance. Data taken at zero magnetic field is marked with 'x' symbols, while data taken at non-zero magnetic fields are marked with 'o' symbols. In the two examples shown in the upper two plots, we see that the zero and finite magnetic field data closely coincide. The lower plot shows measured noise versus sample resistance for various temperatures. The functional form that determines this curve is determined by the impedance matching circuit, as described in [1]. Over the resistance range 600–750 Ω, we observe that the zero and finite magnetic field data overlap precisely, showing that the magnetic field has no effect on our noise measurement circuit.

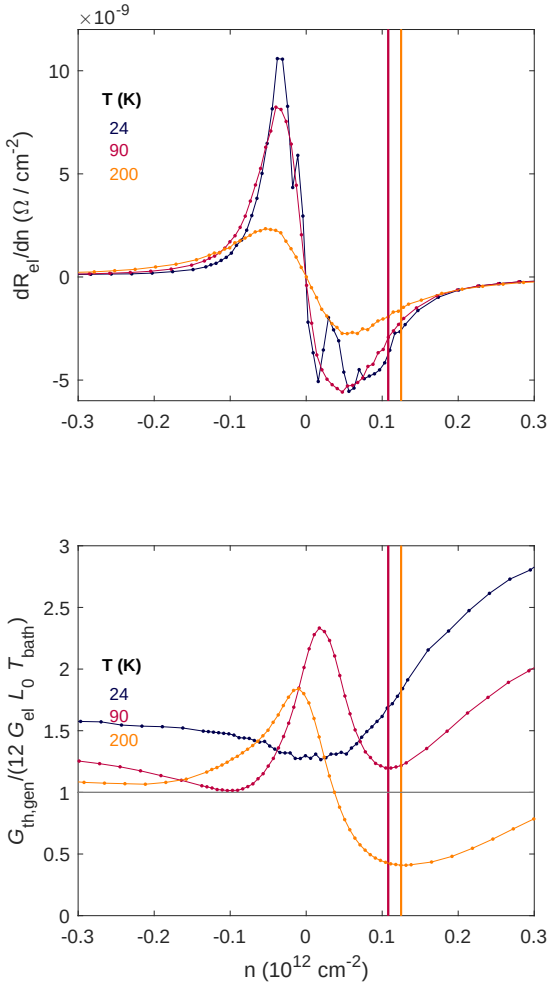

FIG. S9. Density derivative of the electrical resistance versus density. The minimum in the derivative is observed not to coincide with the minimum in the transport ratio at $B = 0$.

V. DENSITY DERIVATIVE OF THE RESISTANCE

Figure S9 compares the density derivative of the electrical resistance to the $B = 0$ transport ratio. The position of the transport ratio minimum at $T_{bath} = 90$ and $200K$, where the minimum exists, is shown to be both temperature dependent, and distinct from the minimum in the density-derivative of the electrical resistance, showing these quantities are not connected.

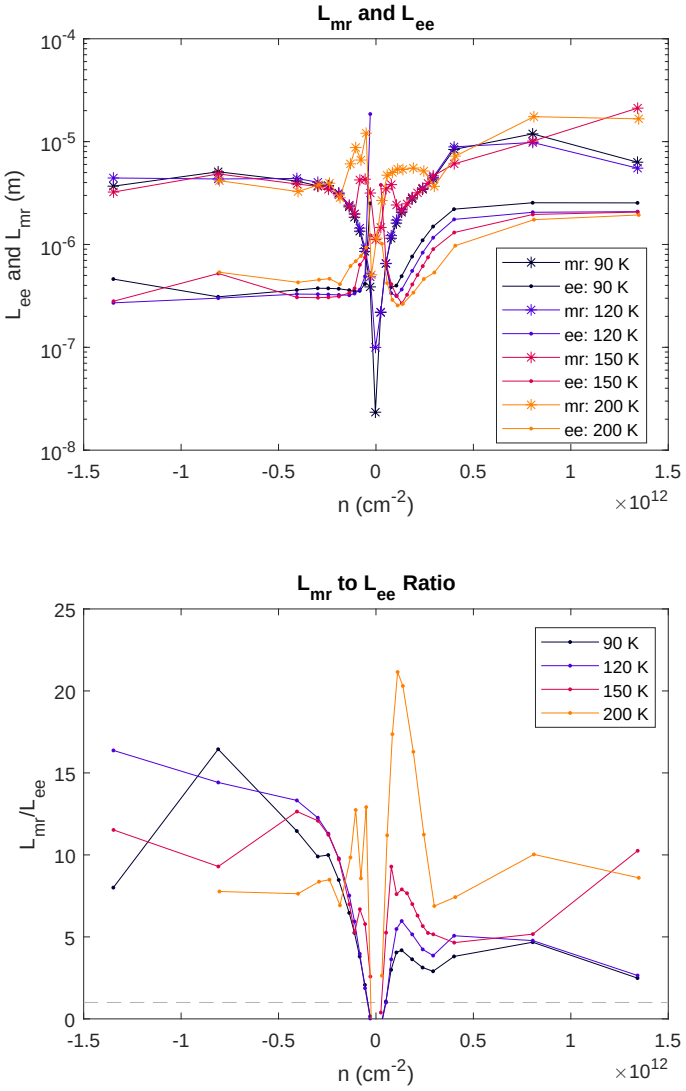

FIG. S10. Momentum-relaxing length scale L_{mr} and momentum-conserving electron-electron scattering length L_{ee} versus density for several T_{bath}, as extracted from the theory fits. Consistent with a hydrodynamic picture, $L_{ee} < L_{mr}$ throughout the non-zero density range. Lengths computed via $L_{ee,mr} = v_F/\gamma_{ee,mr}$, where γ_{mr} comes directly from the fit parameters, and γ_{ee} is obtained from the bulk Lorenz ratio via $\gamma_{ee} = \gamma_{mr} \cdot ([L/L_0]^{-1} - 1)$. from Ref.[2].

VI. MOMENTUM-CONSERVING AND MOMENTUM-RELAXING LENGTH SCALES

Figure S10 shows the momentum-conserving and -relaxing length scales as computed from the theory fits (see main text). The upper panel shows the absolute values of the two length scales, while the lower panel shows their ratio. As expected for the hydrodynamic regime, the momentum-conserving length scale is far shorter than the momentum-relaxing length scale throughout the regime where the Lorenz ratio is suppressed in main text Figure 5. This demonstrates self-consistency of the theory.

VII. $n = 0$ BEHAVIOR AND EVIDENCE FOR THE DIRAC FLUID REGIME

In this section we discuss the zero density behavior observed in Figure 1 of the main text. At $T \approx 90\,K$ there develops a small peak at charge neutrality in the measured transport ratio, decreasing to a slightly smaller value by 200 K. The magnitude of the peak is consistent with both a weak hydrodynamic enhancement[2**?** –7] and a bipolar diffusion enhancement[8, 9], but our experiment cannot measure their relative contributions. Typically, bipolar diffusion effects grow with temperature, but this peak weakens from 90 K to 200 K, consistent with a hydrodynamic enhancement at 90 K getting suppressed by additional electron-phonon energy loss at higher temperatures, as was observed in Ref. [10] where the Lorentz ratio also decreases with T above its peak in a non-monotonic fashion distinct from bipolar diffusion behavior. Here, the value of the peak enhancement is lower and occurs at a different temperature, which could be explained by $\sim 10\times$ larger disorder in this device compared to the cleanest device in Ref. [10]. This is because additional disorder will increase the temperature at which the crossover from the charge puddle to the Dirac Fluid regime occurs, simultaneously weakening the effect which must compete with electron-phonon eneryg loss at higher temperatures.

VIII. TRANSPORT RATIO IN THE BALLISTIC REGIME AT $B = 0$ IN A CONTACT RESISTANCE MODEL

In the ballistic regime, our self-heating Johnson noise thermometry measurement technique produces artificially enhanced transport ratios. This is different from the behavior predicted for a diffusive channel whose resistance is dominated by contact resistance, where the measured transport ratio would trend towards the transport ratio of the contact resistance itself, presumed to be $\frac{\mathcal{L}_c}{\mathcal{L}} = 1$[11]. Here, we present a more generalized version of the contact resistance model developed in Ref. 11.

The total sample resistance is $R_s + 2R_c$, where R_s is the main channel resistance and R_c is each contact resistance. For simplicity, we assume that each contact resistance is line-like [12], and thus there is no temperature gradient in the contact. We use T_0 to denote the bath temperature.

We wish to obtain a formula that gives us the measured transport number $\mathcal{L}_m$ as a function of the sample transport number $\mathcal{L}_s$ and the contact resistance transport number $\mathcal{L}_c$, as well as other fixed or known parameters in the system, including resistance. Most generally, we can write the generalized thermal conductance of the sample, using the total

Joule power P and the average Johnson noise temperature rise $\overline{\Delta T}$, as

$$G_{th,gen} = P/\overline{\Delta T} = \frac{I^2 \left(R_s + 2R_c\right)^2}{R_s\overline{\Delta T_s} + 2R_c\overline{\Delta T_c}}, \tag{1}$$

where $\overline{\Delta T_s}$ and $\overline{\Delta T_c}$ are respective average Johnson noise temperature rises of the sample channel and contact above T_0.

We define the contact resistance R_c to have a thermal resistance $R_{c,th} = 1/G_{th,c}$ such that the temperature drop ΔT_{cs} across the contact resistance is related to the heat Q_c that flows through it via

$$\Delta T_{cs} = \frac{Q_c}{G_{th,c}}, \tag{2}$$

and we can likewise define a contact transport number as

$$\mathcal{L}_c = \frac{G_{th,c}R_c}{T_0}. \tag{3}$$

For the purposes of this model, we will assume, without rigorous justification, that the average Johnson noise temperature of the contact resistance is one half of ΔT_{cs}. This would be the case for a spatially extended uniformly resistive contact resistance, as in Ref. 11. We proceed using the same model for the 1D contact to encapsulated graphene [12].

Ref. 11 assumed that the Joule heat generated at each contact is distributed equally on each side of the contact resistance; the half that goes into the metal contact is immediately thermalized to the bath temperature, and the half that goes into the graphene channel flows through the contact resistor and causes a temperature increase. Here, instead of assuming that the contact resistance Joule power is equally distributed on each side, we will instead assume that a fraction α is distributed on the graphene side, and $1 - \alpha$ is distributed towards the metal contact. In the case of a ballistic device, we typically expect $\alpha \to 0$ because dissipation occurs inside the metal contact (reservoir) itself after the electrons leave the sample.

We will write $\overline{\Delta T_c} = \frac{1}{2}\Delta T_{cs}$ in terms of the total electrical current and the contact transport number. The heat current Q_c flowing through each contact resistance is then half of the heat generated in the channel R_s added to the fraction α of heat generated in the contact resistance R_c:

$$Q_c = \frac{1}{2}I^2R_s + \alpha I^2 R_c. \tag{4}$$

We then obtain

$$\overline{\Delta T_c} = \frac{1}{2}\Delta T_{cs} = \frac{1}{2}\frac{Q_c}{G_{th,c}} = \frac{1}{2}\frac{\frac{1}{2}I^2R_s + \alpha I^2 R_c}{\mathcal{L}_c T_0/R_c}\Delta T_{cs} = \frac{1}{2}I^2\frac{R_c}{\mathcal{L}_c T_0}\left(R_s + 2\alpha R_c\right). \tag{5}$$

The effective bath temperature for the channel becomes $T_0 + \Delta T_{cs}$. We can define an effective self-heating average Johnson noise temperature rise for just the channel, above the effective bath temperature, as

$$\widetilde{\Delta T_s} = \overline{\Delta T_s} - \Delta T_{cs} = \frac{I^2 R_s}{G_{th,gen,s}} = \frac{I^2 R_s}{12 T_0 \mathcal{L}_s / R_s} \tag{6}$$

where $G_{th,gen,s}$ is the generalized thermal conductance of the sample channel only, using the sample transport ratio $\mathcal{L}_s = \dfrac{G_{th,gen,s} R_s}{12 T_0}$. This allows us to write

$$\overline{\Delta T_s} = \Delta T_{cs} + \frac{I^2 R_s^2}{12 T_0 \mathcal{L}_s}. \tag{7}$$

Substituting Eqs. 5 into 7 and into **??**, and the results into Eq. 1, and re-arranging, we obtain

$$G_{th,gen} = \frac{\left(R_s + 2R_c\right)^2}{\dfrac{R_s^3}{12 T_0}\dfrac{1}{\mathcal{L}_s} + \dfrac{R_c}{2T_0}\left(R_s + 2\alpha R_c\right)\left(R_s + R_c\right)\dfrac{1}{\mathcal{L}_c}}. \tag{8}$$

Finally, relating $G_{th,gen}$ to the measured transport ratio as

$$G_{th,gen} = \frac{12 T_0 \mathcal{L}_m}{R_s + 2R_c}, \tag{9}$$

we can write Eq. 8 as

$$\mathcal{L}_m = \frac{\left(R_s + 2R_c\right)^3}{\dfrac{R_s^3}{\mathcal{L}_s} + \dfrac{6R_c\left(R_s + 2\alpha R_c\right)\left(R_s + R_c\right)}{\mathcal{L}_c}}. \tag{10}$$

In the ballistic limit, we have $\alpha \to 0$. Microscopically, this corresponds to electron scattering and randomizing their momenta only once in the large reservoirs (corresponding to the metal contacts in our device) of the ballistic wire model. Applying this limit and re-arranging, we find the measured transport ratio becomes

$$\mathcal{L}_m = \mathcal{L}_s \frac{\left(R_s + 2R_c\right)^3}{R_s^3 + 6R_c R_s\left(R_s + R_c\right)\dfrac{\mathcal{L}_s}{\mathcal{L}_c}}. \tag{11}$$

Expanding Eq. 11 in $\dfrac{R_s}{R_c} \to 0$ (as occurs in a quasi-ballistic or ballistic system), we obtain to the lowest two orders

$$\mathcal{L}_m \approx \mathcal{L}_c \cdot \frac{4}{3}\frac{R_c}{R_s}\left(1 + \frac{1}{2}\frac{R_s}{R_c}\right), \tag{12}$$

showing how the measured transport ratio will become large in ballistic samples where $R_c >> R_s$.

---

[1] A. V. Talanov, J. Waissman, T. Taniguchi, K. Watanabe, and P. Kim, High-bandwidth, variable-resistance differential noise thermometry, Review of Scientific Instruments **92**, 014904 (2021).

[2] A. Lucas and S. D. Sarma, Electronic hydrodynamics and the breakdown of the wiedemann-franz and mott laws in interacting metals, Physical Review B **97**, 10.1103/physrevb.97.245128 (2018).
[3] M. Zarenia, A. Principi, and G. Vignale, Disorder-enabled hydrodynamics of charge and heat transport in monolayer graphene, 2D Materials **6**, 035024 (2019).
[4] A. Lucas, J. Crossno, K. C. Fong, P. Kim, and S. Sachdev, Transport in inhomogeneous quantum critical fluids and in the dirac fluid in graphene, Physical Review B **93**, 10.1103/physrevb.93.075426 (2016).
[5] S. Li, A. Levchenko, and A. V. Andreev, Hydrodynamic electron transport near charge neutrality, Physical Review B **102**, 10.1103/physrevb.102.075305 (2020).
[6] Y. Seo, G. Song, C. Park, and S.-J. Sin, Small fermi surfaces and strong correlation effects in dirac materials with holography, Journal of High Energy Physics **2017**, 10.1007/jhep10(2017)204 (2017).
[7] H.-Y. Xie and M. S. Foster, Transport coefficients of graphene: Interplay of impurity scattering, coulomb interaction, and optical phonons, Physical Review B **93**, 10.1103/physrevb.93.195103 (2016).
[8] H. Yoshino and K. Murata, Significant enhancement of electronic thermal conductivity of two-dimensional zero-gap systems by bipolar-diffusion effect, Journal of the Physical Society of Japan **84**, 024601 (2015).
[9] Y.-T. Tu and S. D. Sarma, Wiedemann-franz law in graphene, Physical Review B **107**, 10.1103/physrevb.107.085401 (2023).
[10] J. Crossno, J. K. Shi, K. Wang, X. Liu, A. Harzheim, A. Lucas, S. Sachdev, P. Kim, T. Taniguchi, K. Watanabe, T. A. Ohki, and K. C. Fong, Observation of the dirac fluid and the breakdown of the wiedemann-franz law in graphene, Science **351**, 1058 (2016).
[11] K. C. Fong, Impact of contact resistance in lorenz number measurements (2017).
[12] L. Wang, I. Meric, P. Y. Huang, Q. Gao, Y. Gao, H. Tran, T. Taniguchi, K. Watanabe, L. M. Campos, D. A. Muller, J. Guo, P. Kim, J. Hone, K. L. Shepard, and C. R. Dean, One-dimensional electrical contact to a two-dimensional material, Science **342**, 614 (2013).